

Minkowski Functionals of CMB polarisation intensity with Pynkowski: theory and application to Planck data

Alessandro Carones,^{1,2*} Javier Carrón Duque,^{1,2} Domenico Marinucci,³ Marina Migliaccio,^{1,2} Nicola Vittorio^{1,2}

¹*Dipartimento di Fisica, Università di Roma “Tor Vergata”, via della Ricerca Scientifica 1, I-00133, Roma, Italy*

²*Sezione INFN Roma 2, via della Ricerca Scientifica 1, I-00133, Roma, Italy*

³*Dipartimento di Matematica, Università di Roma Tor Vergata, via della Ricerca Scientifica 1, I-00133, Roma, Italy*

Accepted XXX. Received YYY; in original form ZZZ

ABSTRACT

The analysis of the Cosmic Microwave Background (CMB) has yielded very precise information about the composition and evolution of the Universe, especially thanks to the study of its Angular Power Spectrum. However, this quantity is blind to the presence of non-Gaussianities and deviations from statistical isotropy; the study of these effects can be performed with other statistics such as Minkowski Functionals (MFs). These tools have been largely applied to the CMB temperature data without any significant detection of a deviation from Gaussianity and isotropy for this field. In this work, we extend the formalism of MFs to the squared CMB polarisation intensity, $P^2 = Q^2 + U^2$. We use the Gaussian Kinematic Formula to analytically determine the theoretical predictions of MFs for a Gaussian isotropic field. We then develop a software which computes these quantities on P^2 Healpix maps and apply it to simulations in order to verify the robustness of both theory and methodology. Finally, we compute the MFs of Planck P^2 maps and compare them with the ones from realistic simulations which include CMB and systematics. We find no significant deviations from primordial Gaussianity or isotropy in Planck CMB polarisation data. However, MFs could play an important role in the analysis of statistical properties of polarised CMB signal from upcoming observations with improved sensitivity. We publicly release the software to compute MFs in arbitrary scalar Healpix maps as a Python package called *Pynkowski*. It is modular, fully documented, and designed to be easy to use in different applications.

Key words: cosmic background radiation – methods: statistical – cosmology: observations – software: public release

1 INTRODUCTION

A wide variety of powerful statistical and geometrical tools have been adopted for the analysis of Cosmological data. Among them, the angular power spectrum of the anisotropies of the Cosmic Microwave Background (CMB) has played a key role in constraining the values of the parameters of the Λ CDM cosmological model, both in temperature and polarisation (Planck Collaboration 2020c). The angular power spectrum contains all the statistical information of a Gaussian isotropic field, but it is blind to the presence of non-Gaussianities or physical anisotropies in the data; in other words, two observed maps can have the same angular power spectrum but still have widely different statistical properties.

The presence of small non-Gaussianities or anisotropies in the primordial Universe is an active field of research as they could encode information about Cosmic Inflation and the very Early Universe, if detected (Bartolo et al. 2004; Pitrou et al. 2008; Barrow & Hervik 2006). Such effects, however, are not associated only to the physics of the primordial Universe: CMB maps are contaminated by foregrounds and affected by CMB lensing, which can induce significant deviations from the Gaussianity and isotropy hypotheses. These signals contain relevant information which is not reflected on the angular power spectrum and has already been proven to help with constrain-

ing cosmological parameters (Zürcher et al. 2021; Chen 2010; Chen et al. 2020; Grewal et al. 2022).

Recently, many studies about primordial non-Gaussianity have also involved the analysis of the Large Scale Structure of the Universe (Andrews et al. 2022; Peña & Candlish 2022). In particular, the power spectrum of galaxy clustering with future galaxy surveys could improve the constraints on primordial non-Gaussianity (Desjacques & Seljak 2010).

Minkowski Functionals (MFs) are one of the most popular tools used to analyse complementary information to the one contained in the angular power spectrum. MFs have been widely explored in the mathematical literature (Tomita 1986; Coles & Barrow 1987; Gott et al. 1990), and have become a popular tool in CMB analysis after the discussion by Schmalzing & Górski (1998).

In the case of scalar Gaussian isotropic fields such as the CMB temperature anisotropies, the theoretical predictions of these functionals can be accurately computed. Given their low variance, any deviation from Gaussianity or statistical isotropy can be detected at high significance in a model-independent manner. MFs are now widely used to measure possible deviations from primordial Gaussianity (Planck Collaboration 2020d) and, beyond that, e.g., to constrain cosmological parameters (Zürcher et al. 2021). However, MFs remain mostly unexploited in the analysis of spin fields, such as CMB polarisation. Therefore, in this work we aim to extend the formalism of MFs to the squared modulus of the CMB polarisation, $P^2 = Q^2 + U^2$,

* E-mail: alessandro.carones@roma2.infn.it

which hereafter we will refer to simply as polarisation modulus or polarised intensity. Planck CMB polarisation maps are dominated by the anisotropic observational strategy, we expect these tools to grow in importance for the analysis of data with much greater sensitivity from on-going or future sub-orbital and satellite experiments such as ACT (Aiola et al. 2020), SPT (Sayre et al. 2020), LSPE (Adamo et al. 2021), Simons Observatory (Ade et al. 2019), CMB-S4 (Abazajian et al. 2022) and LiteBIRD (Matsumura et al. 2014).

This paper has 3 key goals:

- (i) to introduce and generalise the formalism needed to compute the theoretical predictions of scalar maps, such as the CMB temperature anisotropies (T),
- (ii) to apply this extended formalism to obtain the expected values of the MFs of the modulus of a spin field, such as the CMB polarisation (P^2) in the case of Gaussianity and statistical isotropy,
- (iii) to provide the community with a public Python package called Pynkowski¹ in order to easily compute MFs on Healpix maps and compute their Gaussian isotropic expectations.

We note that, up to second-order terms, theoretical predictions of MFs for the sum of two squared Gaussian fields have been already presented in the literature (see Naselsky & Novikov 1998, and the references therein). However, in this work these results are further justified and are derived by means of a more general approach. Furthermore, for the first time these predictions are compared with realistic CMB simulations and the MFs of the P^2 field are computed on Planck data. We also present, to our knowledge, the first public software needed to compute these MFs on any Healpix map.

The structure of this article is as follows. In Section 2 we present the definition of MFs and their application to stochastic fields defined on the sphere. In Section 3 we derive the theoretical expectations of the MFs for CMB polarised intensity: $P^2 = Q^2 + U^2$. In Section 4 we present the Pynkowski Python package and explain the implemented procedures to compute these statistical tools on the maps. In Section 5 we introduce the data and simulations we use in this paper. In Section 6 we present the results of applying this framework and software to CMB polarisation simulations and Planck observations. Finally, in Section 7 we report our conclusions.

2 MINKOWSKI FUNCTIONALS ON THE SPHERE

Minkowski Functionals (MFs) on the sphere are now well-established tools for CMB data analysis (Planck Collaboration 2020d); however, we will first recall some background notation and definitions in order to make the comparison with our present work more explicit.

Given a scalar random field $f(\cdot)$ observed on the unit sphere \mathbb{S}^2 (e.g., CMB temperature anisotropies), the excursion set at a threshold u is defined by

$$A_u(f(\cdot), \mathbb{S}^2) = \{x \in \mathbb{S}^2 : f(x) \geq u\}.$$

We will omit the arguments of A_u to refer to the excursion sets when f and the domain of f are clear by context.

As recalled in Schmalzing & Górski (1998), the morphological properties of these excursion sets can be summarised by the three

MFs defined as follows:

$$\begin{aligned} V_0(A_u) &= \int_{A_u} dx, \\ V_1(A_u) &= \frac{1}{4} \int_{\partial A_u} dr, \\ V_2(A_u) &= \frac{1}{2\pi} \int_{\partial A_u} \kappa(r) dr, \end{aligned}$$

where dr denotes a line element along the boundary of the excursion set and $\kappa(\cdot)$ denotes the geodesic curvature of said boundary. Thus, V_0 represents the excursion area, while V_1 is one fourth of the boundary length.

V_2 is associated with the number of connected regions minus the number of holes, which on the plane corresponds to the Euler–Poincaré characteristic χ . On a spherical surface the Euler–Poincaré characteristic does no longer correspond exactly to V_2 , but includes an extra term which can be computed by means of the generalized Gauss–Bonnet Theorem, which yields:

$$\chi(A_u) = V_2(A_u) + \frac{1}{2\pi} V_0(A_u).$$

From the mathematical point of view, it turns out to be notationally more convenient to replace MFs with the equivalent notion of Lipschitz–Killing Curvatures, which are defined by

$$\begin{aligned} \mathcal{L}_2(A_u) &= V_0(A_u), \\ \mathcal{L}_1(A_u) &= 2V_1(A_u), \\ \mathcal{L}_0(A_u) &= \chi(A_u). \end{aligned}$$

Let us now recall how to compute the expected values of these statistical quantities for Gaussian isotropic maps. These results are well-known in the Cosmological literature in the case of the two-dimensional sphere, but it is convenient to recall them from a more general perspective.

We start by defining μ as the derivative of the covariance function at the origin for the field $f(\cdot)$; we have:

$$\mu = \sum_{\ell} \frac{\ell(\ell+1)}{2} \frac{2\ell+1}{4\pi} C_{\ell},$$

where the sequence $\{C_{\ell}\}$ denotes, as usual, the angular power spectrum of the field $f(\cdot)$. Furthermore, following Adler & Taylor (2007) we define the *flag* coefficients as

$$\left[\begin{matrix} k+j \\ k \end{matrix} \right] = \frac{\omega_{k+j}}{\omega_k \omega_j} \left(\begin{matrix} k+j \\ k \end{matrix} \right), \quad \omega_j = \frac{\pi^{j/2}}{\Gamma(\frac{j}{2}+1)},$$

with $\omega_1 = 2$, $\omega_2 = \pi$, $\omega_3 = \frac{4\pi}{3}$. In general, ω_j represents the volume of the j -dimensional unit ball. For an isotropic Gaussian field, the expected value of the Lipschitz–Killing Curvatures on the sphere is then given by the Gaussian Kinematic Formula (GKF):

$$\mathbb{E}[\mathcal{L}_j(A_u)] = \sum_{k=0}^{2-j} \left[\begin{matrix} k+j \\ k \end{matrix} \right] \rho_k(u) \mathcal{L}_{k+j}(\mathbb{S}^2) \mu^{k/2}, \quad (1)$$

where

$$\begin{aligned} \rho_k(u) &= \frac{1}{(2\pi)^{k/2}} \frac{1}{\sqrt{2\pi}} \exp\left(-\frac{u^2}{2}\right) H_{k-1}(u), \\ H_{-1}(u) &= 1 - \Phi(u), \\ H_0(u) &= 1, \\ H_1(u) &= u, \end{aligned}$$

and in general, $H_k(u) = (-1)^k \exp\left(\frac{u^2}{2}\right) \frac{d^k}{du^k} \exp\left(-\frac{u^2}{2}\right)$ denotes the

¹ <https://github.com/javicarron/pynkowski>

sequence of Hermite polynomials. The function Φ is the cumulative normal distribution.

In particular, by [equation \(1\)](#) we get the well-known results for the expected values of the Lipschitz–Killing Curvatures and, hence, of MFs, which we report normalised by area. In order, we have:

$$\mathbb{E}[\mathcal{L}_2(A_u)] = \rho_0(u)\mathcal{L}_2(\mathbb{S}^2) = 4\pi\{1 - \Phi(u)\},$$

$$\frac{\mathbb{E}[V_0]}{4\pi} = 1 - \Phi(u).$$

We note that this quantity depends only on u , not on the field itself as long as it is normalised to have unit variance.

Likewise:

$$\begin{aligned}\mathbb{E}[\mathcal{L}_1(A_u)] &= 2\frac{\omega_2}{\omega_1^2}\rho_1(u)\mathcal{L}_2(\mathbb{S}^2)\mu^{1/2} \\ &= \frac{2\pi}{4}\frac{1}{(2\pi)^{1/2}}\frac{1}{\sqrt{2\pi}}\exp\left(-\frac{u^2}{2}\right)4\pi\mu^{1/2} \\ &= \exp\left(-\frac{u^2}{2}\right)\pi\mu^{1/2}\end{aligned}$$

so that

$$\frac{\mathbb{E}[V_1]}{4\pi} = \frac{1}{8}\exp\left(-\frac{u^2}{2}\right)\mu^{1/2}.$$

Finally:

$$\begin{aligned}\mathbb{E}[\mathcal{L}_0(A_u)] &= \rho_0(u)\mathcal{L}_0(\mathbb{S}^2) + \rho_2(u)\mathcal{L}_2(\mathbb{S}^2)\mu \\ &= \{1 - \Phi(u)\}2 + \frac{2}{\sqrt{2\pi}}\mu\exp\left(-\frac{u^2}{2}\right)u,\end{aligned}$$

and hence:

$$\frac{\mathbb{E}[V_2]}{4\pi} = \frac{1}{\sqrt{(2\pi)^3}}\mu\exp\left(-\frac{u^2}{2}\right)u.$$

The interpretation of the previous formulae is worth discussing: the expected values of the MFs (and Lipschitz–Killing Curvatures) are expressed by means of a product of four different independent ingredients:

- (i) a set of universal coefficients (called “flag” coefficients),
- (ii) the Lipschitz–Killing Curvatures evaluated on the original manifold (in our case, the unitary sphere),
- (iii) a power of the derivative of the covariance function of the field at the origin,
- (iv) a set of “density” functions ρ_k , dependent only on the threshold at which the MFs (or Lipschitz–Killing Curvatures) are evaluated.

The remarkable fact is that in the case of polarisation, the expected values for Lipschitz–Killing Curvatures take exactly the same form—the only change is in the “density” functions ρ_k , which nonetheless can be expressed with a fully explicit analytic form. We give more details in the section to follow.

We also note that the presence of a mask only affects the manifold where the map is defined, and therefore only affects the normalisation of the MFs.

3 MINKOWSKI FUNCTIONALS ON POLARISATION FIELDS

A spin s random field P_s is a complex-valued field that satisfies the following relation at any fixed point x :

$$P'_s(x) = \exp(is\theta)P_s(x).$$

where $P'(\cdot)$ represents the value in $x \in \mathbb{S}^2$ when the local coordinates are rotated by an angle θ .

This notion can be made mathematically rigorous viewing spin fields as a section of a so-called spin fiber bundle, first introduced in mathematical physics by [Newman & Penrose \(1966\)](#).

Under this definition, the CMB polarisation is a Gaussian complex-valued spin-2 random field, that can be written as:

$$P(x) = Q(x) + iU(x), \quad P'(x) = \exp(i2\theta)P(x),$$

where Q and U are real fields.

It is important to note that, for any fixed choice of a coordinate system, polarisation fields can be viewed as complex-valued Gaussian random variables at a single point, but they can no longer be considered as the realisation of an isotropic map. Indeed the correlation function at any two points is not invariant to rotations, and hence it does not only depend on the geodesic distance between the two points (as required by isotropy). Only in the special case where $s = 0$, we are back to the case of a complex-valued isotropic Gaussian map, which can always be viewed as the complexification of two Gaussian independent and identically distributed real-valued fields Q and U .

The behaviour of the expected values for Lipschitz–Killing Curvatures and other topological functionals of spin fields has been very recently investigated in the mathematical literature by [Lerario et al. \(2022\)](#). The main finding of these authors is that for “band-limited” spin-valued random fields with power spectrum concentrated around multipoles equal or larger than ℓ_* , the effect of the spin vanishes as ℓ_* grows. In that case, these geometric functionals have the same behaviour for spin Gaussian fields and for complex-valued scalar Gaussian fields. More precisely, the remainder terms (neglected when approximating the geometry of a spin $s \neq 0$ field with the spin $s = 0$ case) are of the form $\propto \frac{s}{\ell(\ell+1)}$. Thus, spin effects can be safely ignored for the random fields of cosmological interest, as there is very little power at small multipoles. Incidentally, from the mathematical point of view, these results continue to hold for any fixed value of the spin parameter s , and even under other conditions such as the (non-physical) case of a spin parameter growing with ℓ_* .

We can informally summarise this mathematical result as follows:

Up to negligible terms which depend only on the smallest multipoles, the expected values of the Lipschitz–Killing Curvatures for the excursion sets of the norms of spin s random fields are identical, for all values of s . In other words, defining

$$|P_s(x)|^2 := Q_s^2(x) + U_s^2(x),$$

we have that

$$\mathbb{E}\left[\mathcal{L}_j(A_u(|P_s(\cdot)|^2, \mathbb{S}^2))\right] = \mathbb{E}\left[\mathcal{L}_j(A_u(|P_0(\cdot)|^2, \mathbb{S}^2))\right],$$

for all values of j and s .

We are now going to derive the expected values of Lipschitz–Killing Curvatures using the GKF, in an analogous way to the previous Section. It should be noted that, up to second-order terms, results equivalent to ours have been given before in the literature, see [Kasak et al. \(2021\)](#), [Naselsky & Novikov \(1998\)](#), and the references therein. Apart from putting these results into more solid grounds by means of the approximation that we just explained, we believe that our derivation by means of the GKF is clearer and more amenable to generalisations.

In particular, assume that we have Q and U two independent copies of Gaussian random fields with the same angular power spectrum, expected value 0 and variance normalised to 1 (e.g. $\mathbb{E}[Q^2(x)] =$

$\mathbb{E}[U^2(x)] = 1$). Defining

$$P^2(x) = Q^2(x) + U^2(x),$$

it is immediate to demonstrate that $P^2(\cdot)$ is a chi-squared with two degrees of freedom, $P^2(\cdot) \sim \chi^2_2$, and hence it has marginal density

$$f_{P^2}(u) = \frac{1}{2} \exp\left(-\frac{u}{2}\right).$$

We are now considering again the excursion sets

$$A_u(P^2(\cdot), \mathbb{S}^2) = \left\{x \in \mathbb{S}^2 : P^2(x) \geq u\right\}.$$

We can now recall again the GKF, which in the case of chi-square fields reads

$$\begin{aligned} \mathbb{E}[\mathcal{L}_j(A_u(P^2(\cdot), \mathbb{S}^2))] &= \\ &= \sum_{k=0}^{d-j} \left[\begin{matrix} k+j \\ k \end{matrix} \right] \rho_{k;P^2}(u) \mathcal{L}_{k+j}(\mathbb{S}^2) \mu^{k/2}, \end{aligned} \quad (2)$$

where as usual we write μ for the derivative of the covariance function evaluated at the origin. It should be noted that the expression for the expected values takes exactly the same form as in [equation \(1\)](#), simply replacing the functions $\rho_k(\cdot)$ with $\rho_{k;P^2}(\cdot)$ defined by [Adler & Taylor \(2007, Theorem 15.10.1\)](#):

$$\begin{aligned} \rho_{j,P^2}(u) &= \frac{u^{(k-j)/2} \exp(-u/2)}{(2\pi)^{j/2} \Gamma(k/2) 2^{(k-2)/2}} \\ &\times \sum_{l=0}^{\lfloor \frac{j-1}{2} \rfloor} \sum_{m=0}^{j-1-2l} \mathbb{I}_{\{k \geq j-m-2l\}} \binom{k-1}{j-1-m-2l} \\ &\times \frac{(-1)^{j-1+m+l}}{m!l!2^l} u^{m+l}. \end{aligned}$$

More explicitly, for $j = 1$ we obtain

$$\rho_{1,P^2}(u) = \frac{u^{1/2} \exp(-u/2)}{(2\pi)^{1/2}},$$

whereas for $j = 2$ we have

$$\begin{aligned} \rho_{2,P^2}(u) &= \frac{\exp(-u/2)}{(2\pi)} \sum_{m=0}^1 \binom{1}{1-m} (-1)^{1+m} u^m \\ &= -\frac{\exp(-u/2)}{(2\pi)} + \frac{\exp(-u/2) u}{(2\pi)} \\ &= \frac{(u-1) \exp(-u/2)}{2\pi}. \end{aligned}$$

Plugging these expressions into [equation \(2\)](#) we obtain, for the boundary length,

$$\begin{aligned} \mathbb{E}[2\mathcal{L}_1(A_u(P^2(\cdot), \mathbb{S}^2))] &= \\ &= 2 \sum_{k=0}^{d-j} \left[\begin{matrix} k+j \\ k \end{matrix} \right] \rho_{P^2}(u) \mathcal{L}_{k+j}(\mathbb{S}^2) \sqrt{\mu} \\ &= 2 \left[\begin{matrix} 2 \\ 1 \end{matrix} \right] \frac{u^{1/2} \exp(-u/2)}{(2\pi)^{1/2}} \mathcal{L}_2(\mathbb{S}^2) \sqrt{\mu} \\ &= 4 \frac{\omega_2}{\omega_1^2} \frac{u^{1/2} \exp(-u/2)}{(2\pi)^{1/2}} \cdot 4\pi \cdot \sqrt{\mu} \\ &= 4 \frac{\pi}{4} \frac{u^{1/2} \exp(-u/2)}{(2\pi)^{1/2}} \cdot 4\pi \cdot \sqrt{\mu} \\ &= \frac{\sqrt{2\pi}}{2} u^{1/2} \exp(-u/2) \cdot 4\pi \cdot \sqrt{\mu}. \end{aligned}$$

The excursion area can be immediately computed as:

$$\begin{aligned} \mathbb{E}[\mathcal{L}_2(A_u(P^2(\cdot), \mathbb{S}^2))] &= \mathbb{E}\left[\int_{\mathbb{S}^2} \mathbb{I}(P^2(x) \geq u) dx\right] \\ &= \int_{\mathbb{S}^2} \mathbb{E}[\mathbb{I}(P^2(x) \geq u)] dx \\ &= 4\pi \exp(-u/2). \end{aligned}$$

Finally, for the Euler-Poincaré Characteristic

$$\begin{aligned} \mathbb{E}[\mathcal{L}_0(A_u(P^2, \mathbb{S}^2))] &= \\ &= 2\mu(u-1) \exp(-u/2) + 2 \exp(-u/2). \end{aligned}$$

Converting from the Lipschitz–Killing curvatures to MFs, and normalising by the area of the sphere, we finally obtain the following predictions for a chi-squared map with 2 degrees of freedom such as P^2 :

$$\frac{\mathbb{E}[V_0(A_u)]}{4\pi} = \exp(-u/2) \quad (3a)$$

$$\frac{\mathbb{E}[V_1(A_u)]}{4\pi} = \frac{\sqrt{2\pi}}{8} \sqrt{\mu u} \exp(-u/2) \quad (3b)$$

$$\frac{\mathbb{E}[V_2(A_u)]}{4\pi} = \mu \frac{(u-1) \exp(-u/2)}{2\pi} \quad (3c)$$

where the threshold is non-negative, $u \geq 0$. For negative thresholds, it follows from the definition that V_0 is exactly 1 while V_1 and V_2 are exactly 0. In particular, V_2 presents a discontinuity at $u = 0$ connected with the number of non-polarised points (see [Kasak et al. 2021](#)).

In all these expressions, the variance of the field is unity and μ is the derivative of the covariance of the field at the origin, that is as before:

$$\mu = \sum_{\ell} \frac{2\ell+1}{4\pi} \frac{\ell(\ell+1)}{2} C_{\ell}, \quad \sum_{\ell} \frac{2\ell+1}{4\pi} C_{\ell} = 1,$$

where:

$$C_{\ell} = \frac{1}{2} (C_{\ell}^{EE} + C_{\ell}^{BB}),$$

with C_{ℓ}^{EE} and C_{ℓ}^{BB} , respectively, the EE and BB angular power spectra computed from Q and U maps ([Kamionkowski et al. 1997](#); [Zaldarriaga & Seljak 1997](#)).

4 PYNKOWSKI

We develop a Python package called *Pynkowski* to compute MFs on spherical maps formatted in the HEALPix convention ([Górski et al. 2005](#)). We make this package publicly available to the research community in <https://github.com/javiccarron/pynkowski>.

Pynkowski can be used in two different ways:

(i) To compute the expected values of the MFs for Gaussian scalar fields like CMB temperature anisotropies T (see [Section 2](#)) or for χ^2 fields like CMB polarised intensity P^2 (see [Section 3](#)). They can be computed given either an input angular power spectrum or μ .

(ii) To determine the MFs on any scalar map, either on the full sky or within any mask.

Both T and P^2 are scalar fields on the sphere, and therefore the MFs can be computed with the same code for both quantities, although their expected results are different. We describe the implementation in this section, where we refer generally to an arbitrary (smooth) field on the sphere $f(x)$. We compute the MFs normalised by the

area of the sphere ($v_i = \frac{V_i}{4\pi}$), so the extension to masked maps is straight-forward.

Without loss of generality, for this work we normalise input maps to have unit variance, as we did in the previous sections when computing the theoretical predictions. In the case of P^2 , both the U -map and the Q -map are separately normalised to unit variance. The MFs can now be expressed as a function of the adimensional threshold u .

4.1 Computation of the MFs

First MF, v_0

The first MF, v_0 , is computed according to the equation:

$$v_0(u) = \frac{1}{4\pi} \int_{S^2} \Theta(f(x) - u) dx \quad (4)$$

where $\Theta(r)$ is the Heaviside function (1 where $r \geq 0$; 0 otherwise). In the computation, we approximate the integral with a sum over all valid pixels. The integral divided by the area of the sphere, 4π , can be seen as the average value of the argument inside the integral. Therefore, it can be approximated with the average over all pixels. Thus, $v_0(u)$ is computed as the fraction of pixels above the threshold u .

Second MF, v_1

The second MF, v_1 , is computed according to the equation:

$$\begin{aligned} v_1(u) &= \frac{1}{4\pi} \frac{1}{4} \int_{\partial A_u} dr \\ &= \frac{1}{4\pi} \frac{1}{4} \int_{S^2} \delta(f(x) - u) \cdot |\nabla f| dx \end{aligned} \quad (5)$$

where the second equality is the result of a change of coordinates from the line element dr of the boundary of the excursion set to a surface element dx on the sphere. The gradient of f is denoted by ∇f and δ is the Dirac delta.

We start by computing $|\nabla f|$ at every pixel. Then, in order to approximate the integral with a sum over pixels, we provide a bin of Δu . We create a mask $M_u(x)$ representing the pixels where the value of the map is close to u :

$$M_u(x) = \begin{cases} 1 & \text{if } u - \frac{\Delta u}{2} \leq f(x) \leq u + \frac{\Delta u}{2} \\ 0 & \text{otherwise} \end{cases} \quad (6)$$

Now, $v_1(u)$ can be computed as the mean of the pixels of $M_u \cdot |\nabla f|$, divided over Δu , the bin size, and 4, the normalisation factor.

Third MF, v_2

The third MF, v_2 , is computed according to the equation:

$$\begin{aligned} v_2(u) &= \frac{1}{4\pi} \frac{1}{2\pi} \int_{\partial A_u} \kappa(r) dr \\ &= \frac{1}{4\pi} \frac{1}{2\pi} \int_S \delta(f(x) - u) \cdot |\nabla f| \cdot \kappa dx \end{aligned} \quad (7)$$

The change of coordinates to surface element and the approximation to a finite sum of pixels is analogous to the previous case. We define the mask M_u identically, and compute the mean of the pixels of $M_u \cdot |\nabla f| \cdot \kappa$. This quantity is then divided by the bin size Δu and by 2π to yield the value of $v_2(u)$.

In this formula, κ is the geodesic curvature of the boundary of the excursion set. Given that this curve is given by the implicit equation

$f(x) = u$, we can use the expression of κ for an implicit curve (see, e.g., [do Carmo 1976](#)):

$$\kappa = \frac{2f_{;\phi}f_{;\theta}f_{;\phi\theta} - f_{;\theta}^2f_{;\phi\phi} - f_{;\phi}^2f_{;\theta\theta}}{(f_{;\phi}^2 + f_{;\theta}^2)^{\frac{3}{2}}} \quad (8)$$

where the semicolon denotes the covariant derivative. All the quantities involved in this expression can be computed for each pixel.

4.2 Computation of the derivatives

The spatial derivatives of the maps (both partial and covariant) are computed with the help of the healpy² function `alm2map_der` in harmonic space. The covariant derivatives of a field f on the sphere are computed in terms of the partial derivatives:

$$\begin{aligned} f_{;\theta} &= f_{,\theta} \\ f_{;\phi} &= \frac{f_{,\phi}}{\cos \theta} \\ f_{;\theta\theta} &= f_{,\theta\theta} \\ f_{;\theta\phi} &= \frac{f_{,\theta\phi}}{\cos \theta} - \frac{\sin \theta \cdot f_{,\phi}}{\cos^2 \theta} \\ f_{;\phi\phi} &= -\frac{f_{,\phi\phi}}{\cos^2 \theta} + f_{,\theta} \cdot \tan \theta \end{aligned}$$

where we consider $\theta \in (-\pi/2, \pi/2)$ as the latitude and $\phi \in [0, 2\pi)$ as the longitude.

The need of computing the spatial derivatives of the map means that the computations are reliable only for maps whose angular power spectrum is negligible at multipoles close to $\ell_{max} = 3 \cdot n_{side} - 1$; i.e., the derivatives can only be computed if the maps are reasonably smooth. This becomes a requirement in order to compute v_1 and v_2 , while v_0 can be computed for any map as it does not require the computation of the derivatives.

This smoothness condition is satisfied for realistic T and P^2 maps, as they are reasonably smooth, but it can break if one tries to analyse maps of pure noise or heavily dominated by the smallest scales (pixel-size scales). We note that our theoretical results only hold for functions that are at least twice-differentiable almost everywhere (for other cases, such as a fractal behaviour, see [Lan et al. 2018](#)).

5 SIMULATIONS AND DATA

5.1 Gaussian simulations

In order to validate the implementation of the computation on Healpix maps and the theoretical predictions, we generate 300 Gaussian isotropic CMB maps. We use the healpy function `synfast` with the best fit angular power spectrum for polarisation (E and B modes) as reported by [Planck Collaboration \(2020b\)](#). For these simulations, we fix a resolution of $N_{side} = 1024$; this is half of the Planck value in order to reduce the computational time without a significant loss of resolution; we have verified that the results remain unchanged by this choice.

For the estimation of v_0 , we exclude the modes with $\ell \leq 4$ in the simulated maps in order to avoid spin effects in the computation of the MF (see [Section 3](#)). Conversely, when v_1 and v_2 are estimated, a smoothing of the maps with a Gaussian beam of FWHM= 15' is

² <https://github.com/healpy/healpy>

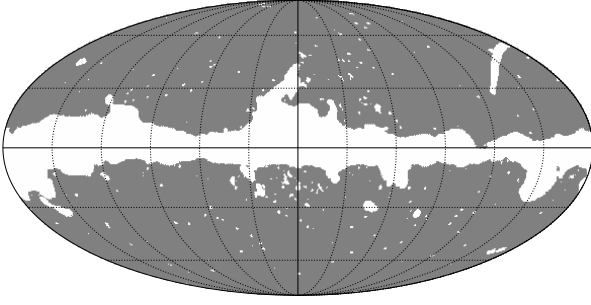


Figure 1. 2018 Component Separation common Planck mask for polarisation. It excludes the most contaminated regions near the Galactic plane and the polarised point sources. It keeps a total sky fraction of $f_{sky} = 78\%$.

applied in order to avoid pixelization effects in the computation of the spatial derivatives.

MFs have been computed over the full sky maps of $P^2 = Q^2 + U^2$, where Q and U have been previously normalised to unit variance. We analyse the deviation of each MF at different values of the threshold u in these simulated realisations of Gaussian isotropic CMB with respect to the theoretical expectations.

In this way, we are able to simultaneously assess the accuracy of the formulae obtained in Section 3 and verify the implementation of MFs computations on simulated maps.

5.2 Planck polarisation maps

After validating the machinery with Gaussian isotropic CMB simulations, we apply the MFs to Planck CMB polarisation data. In order to verify that the results are consistent and do not depend on the component separation algorithm used to reconstruct the CMB, we use the polarisation maps released by the Planck collaboration obtained with two different pipelines: SMICA (Spectral Matching Independent Component Analysis) and SEVEM (Spectral Estimation Via Expectation Maximisation), as reported in Planck Collaboration (2020a).

SMICA (Delabrouille et al. 2003) performs a foregrounds and noise subtraction by linearly combining Planck frequency maps with multipole-dependent weights, up to $\ell = 4000$, which minimise on each angular scale the variance of the output map. In polarisation, it combines the E and B modes independently and then recombine them to report the Q and U maps.

SEVEM (Martínez-González et al. 2003), instead, is a template fitting method. Different templates of the foregrounds emission are estimated by the subtraction of input maps at close Planck frequencies. This procedure removes CMB signal while preserving the Galactic one. A linear combination of these templates is then subtracted from input data to produce a cleaned CMB map at a specific Planck frequency. The coefficients of the linear combination are determined by minimising the variance of the cleaned map outside a mask, that covers the point sources detected in polarisation and the 3% brightest Galactic emission. The 100, 143 and 217 GHz cleaned maps are then combined in harmonic space, using E and B decomposition, to produce the final CMB maps for the Q and U components at a resolution of $\text{FWHM}=5'$ and a maximum considered multipole of $\ell = 3000$.

The native resolution of these released maps is $N_{\text{side}} = 2048$; we degrade them to $N_{\text{side}} = 1024$ in order to exactly match the pipeline applied for simulations. Similarly, we exclude again the lowest multipoles ($\ell \leq 4$) before the computation of V_0 in order to avoid spin effects.

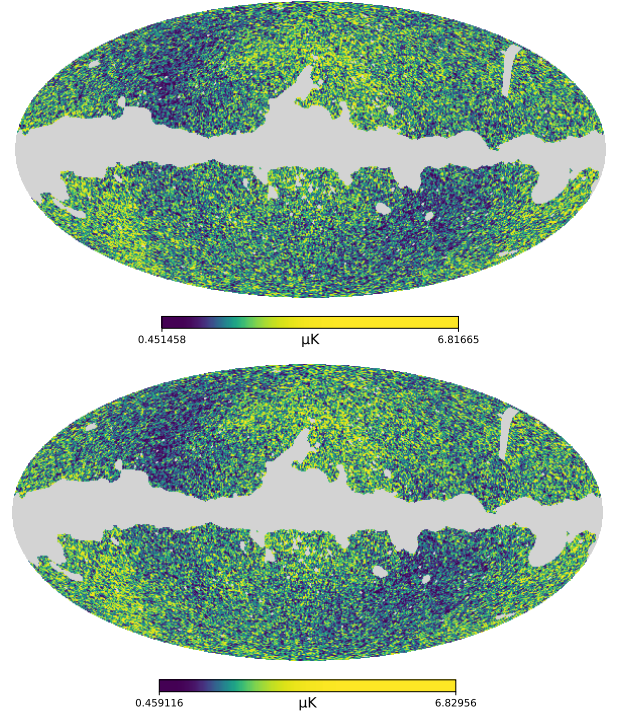


Figure 2. Planck CMB maps for $P = \sqrt{Q^2 + U^2}$ by the SMICA (top) and SEVEM (bottom) pipelines. They have been smoothed with a Gaussian beam of FWHM $30'$ for visualisation purposes.

Planck CMB polarisation maps are still affected by a residual contamination due to Galactic foregrounds and point sources. The most contaminated regions of the sky must be excluded in any cosmological analysis. Therefore, we adopt throughout all the analysis the 2018 Component Separation Common mask in polarisation, as recommended by (Planck Collaboration 2020a) and shown in Figure 1. Such mask was obtained by thresholding the standard deviation between each of the four cleaned Planck CMB maps; this mask is then augmented with the Commander and SEVEM confidence masks, as well as with the SEVEM and SMICA in-painting masks.

The masked SMICA and SEVEM P maps are shown in Figure 2.

5.3 Planck end-to-end simulations

The SMICA and SEVEM maps include residual effects associated to Planck systematics, which are especially relevant in polarisation. These contamination has to be properly taken into account for any cosmological analysis of the Planck CMB maps. To this goal, the Planck collaboration released end-to-end simulations which include the expected CMB signal and noise residuals.

These simulations have been obtained by generating realistic CMB (Gaussian and isotropic) and noise maps at the different Planck frequency channels, which are then processed by each component separation algorithm. The resulting maps are thus able to reflect the expected statistical properties across the sky of CMB and noise residuals given by each method.

We compare the MFs of the SMICA and SEVEM released CMB polarisation maps with the ones computed on these realistic simulations. Compatible results would suggest that all non-Gaussianity and anisotropy present in CMB polarisation maps is compatible with the ones produced by known systematics. A significant deviation would signal the presence of residual non-Gaussian or anisotropic fore-

grounds, unmodeled systematic effects, or a hint of non-Gaussianity or statistical anisotropy of the CMB of primordial origin.

We use both SMICA and SEVEM CMB simulations with $N_{\text{side}} = 1024$ to make all the analysis identical in all maps.

5.4 Compatibility analysis

In order to assess the level of deviation between MFs on different maps, we use the χ^2 statistic. Let X be a vector with the result of any of the MFs with the mean of the simulations subtracted, and Σ the covariance matrix of X (representing the correlation of MFs at different thresholds). The χ^2 statistic is given by:

$$\chi^2 = X^T \Sigma^{-1} X \quad (9)$$

If S is the sample covariance (computed with simulations), an unbiased estimator of the inverse of the covariance is:

$$\Sigma^{-1} = \frac{N - d - 2}{N - 1} S^{-1} \quad (10)$$

where $N = 300$ is the number of simulations and $d = 100$ is the number of bins in the considered range of thresholds u . The prefactor in this equation is known as the Hartlap factor (Hartlap et al. 2007) and it is needed in order for the estimator to be unbiased.

In this analysis we report the reduced $\chi^2 = \chi^2/N_{\text{dof}}$, where $N_{\text{dof}} = 100$ is the number of degrees of freedom (*i.e.*, the number of thresholds in our computation). We also compute the probability-to-exceed a given χ^2 :

$$p_{\text{exc}}(\text{data}) = P(\chi_{\text{sims}}^2 > \chi_{\text{data}}^2) \quad (11)$$

where a value close to 50% means that the data closely resembles the expectation, while a value close to 0% or 100% means that data is highly incompatible with simulations.

Finally, we also report the significance of the deviation of χ^2 in data with respect to the mean and standard deviation of simulations. This is reported in units of σ_{sims} .

6 RESULTS

In this section, we proceed to validate the code and the theoretical formulae for the expected values of the MFs for P^2 maps. We then apply the pipeline to Planck CMB polarisation maps in order to assess the presence of non-Gaussianities or underlying anisotropies.

In Section 6.1, we compare the theoretical expectation of MFs for a $P^2 = Q^2 + U^2$ field under the assumption of Gaussianity and isotropy with the ones computed on CMB simulations generated with the same statistical properties. In Section 6.2, MFs are computed on the Planck SMICA CMB polarisation modulus map and compared with the ones of end-to-end Planck simulations.

6.1 Validation

We verify the theoretical predictions for the MFs of P^2 introduced in Section 3 by comparing them with the results of simulated CMB Gaussian isotropic maps. We simulate 300 such maps as reported in Section 5.1, and compute the MFs on them as explained in Section 4 at thresholds between $u = 0$ and 5, with a spacing of $\Delta u = 0.05$. Maps are generated with a known angular power spectrum, so the value of μ can be exactly computed; we use this value to compute the theoretical expectations of the MFs according to equation (3). As an example, in this section we report the results on simulations generated using the Planck best-fit angular power spectra, but we

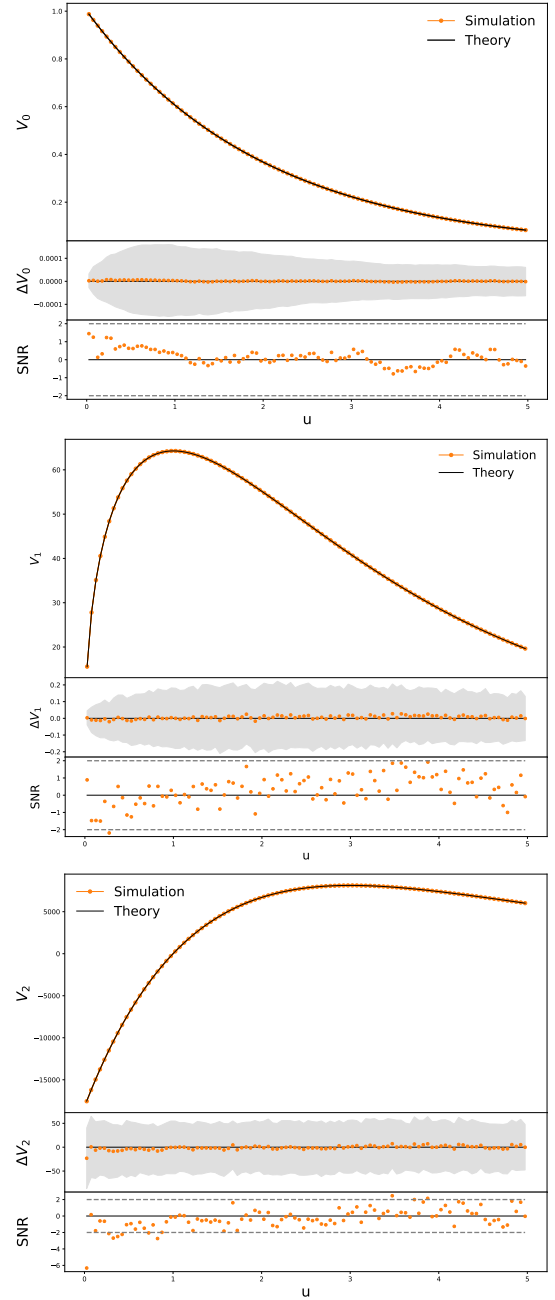


Figure 3. Average Minkowski Functionals of $P^2 = Q^2 + U^2$ for $N_{\text{sims}} = 300$ CMB Gaussian isotropic simulations (orange dots) are compared with the theoretical predictions (solid black lines). From top to bottom: V_0 , V_1 , and V_2 . From top to bottom of each panel: the value of the MF, the residuals between simulations and theory compared with the dispersion among simulations (1σ), and with the deviation of the mean of simulations computed as σ/N_{sims} (see text for details).

verify that the results hold for arbitrary angular power spectra, as long as there is no significant power in the scales corresponding to the pixel size.

The results of the MFs can be seen in Figure 3, along with the theoretical predictions. We find that simulations are fully compatible with the theoretical expectation for all three MFs, with residuals well inside the 1σ region, where σ is the dispersion of the MFs among the 300 simulations.

Additionally, in order to explore any possible systematic deviation, we compare the average residuals on simulations with respect to the theoretical expectations considering the standard deviation of the mean ($\sigma_{\text{mean}} = \frac{\sigma_{\text{sim}}}{\sqrt{300}}$). Such comparison is shown in the bottom rows of the plots in Figure 3. The three MFs are all perfectly compatible with the theory, both in the case of individual simulations and of the average behaviour.

We also note the low statistical variation of these curves: the relative uncertainty of every point is below 1% and, in the case of V_0 , it is below 1 part in 1000. These values of the statistical standard deviation depend on the angular power spectrum of the studied map: we observe that the variance decreases when increasing the maximum multipole considered, ℓ_{max} (*i.e.*, when increasing the resolution of the maps). This is also known to be the case for temperature maps, as quantitatively studied in Fantaye et al. (2015).

These results provide a double validation: on the one hand, they verify the mathematical framework used to predict the expected values of the MFs of P^2 maps; on the other hand, they validate our implementation in the Pynkowski package.

We have verified that masking the maps has a negligible effect on these results beyond slightly increasing the noise due to the smaller sky fraction. This robustness is expected because, unlike the angular power spectrum, MFs are purely local quantities. Thus, the effect of masking is completely negligible.

6.2 Planck 2018 polarisation maps

Once both the theoretical predictions and our implementation to compute MFs have been validated, we can apply this formalism to the observed CMB polarisation maps in order to assess the presence of any non-Gaussianity or deviation from statistical isotropy. We use two different complementary component separation methods in order to verify that the conclusions remain unchanged when producing the maps with different algorithms.

In this work, we analyse the CMB maps reported by Planck (Planck Collaboration 2020a), produced with two different methods: SMICA (shown in this Section) and SEVEM (shown in Appendix A); see Section 5 for details. We verify that our results are consistent on both complementary pipelines.

Planck polarisation maps are affected by two known contaminating signals that would bias our MFs estimates if they are unaccounted for. The first one is the residual emission from the Galactic foregrounds and point sources. In order to minimise their impact, we adopt the 2018 Component Separation Common mask in polarisation (Planck Collaboration 2020a), as shown in Figure 1. The second contaminant is the residual noise whose statistical properties are not homogeneous across the sky due to the observation strategy of the Planck satellite (Planck Collaboration 2011), as it can be seen in Figure 2. This effect is included in the end-to-end simulations provided by the collaboration, as explained in Section 5.3. By comparing Planck released maps to simulations with realistic noise residuals, we can assess possible deviations from Gaussianity and isotropy in the primordial polarised CMB signal. The effect of the anisotropic noise is discussed in Appendix B.

In Figure 4 we report the comparison between the MFs computed on Planck polarisation modulus map and on end-to-end simulations, both produced by SMICA. We see for all MFs a remarkable agreement between them. Only V_0 seems to be consistently below the average values in simulations at high thresholds, but this deviation is small and consistent with a statistical fluctuation.

We quantify the compatibility of all curves in terms of the χ^2

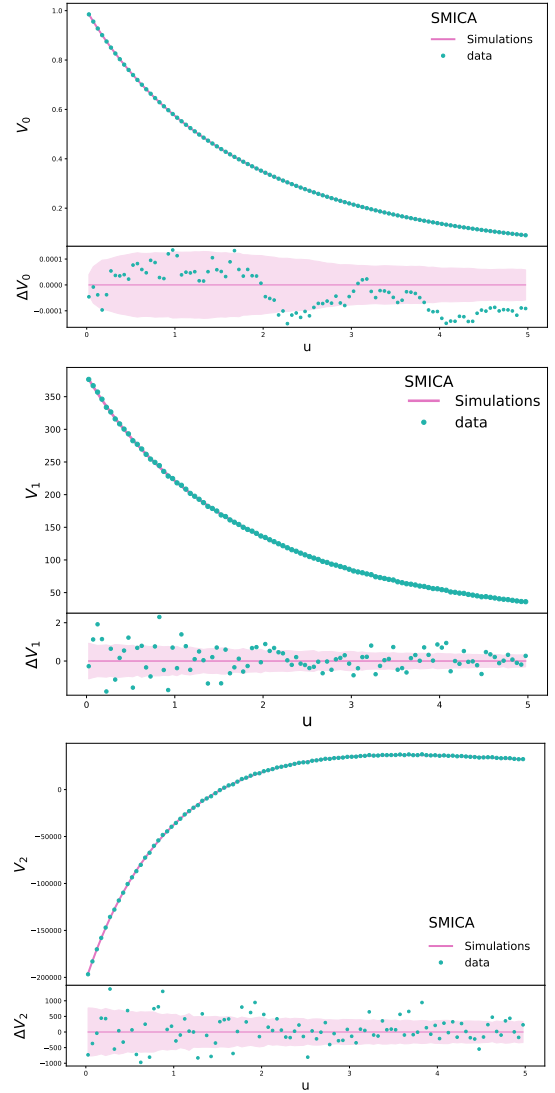


Figure 4. Minkowski Functionals of the Planck SMICA released $P^2 = Q^2 + U^2$ maps (blue dots) are compared with the ones of realistic end-to-end simulations (pink solid line). First, second, and third MFs are shown (top to bottom), with the values and the residual with respect to the mean of simulations. The shaded pink region, representing the $\pm 1\sigma$ region obtained in simulations, is included in all plots.

statistic (as well as the probability to exceed and the deviation with respect to simulations in terms of σ), as explained in Section 5.4. The results can be seen in Table 1 and show that no deviation is statistically significant nor consistently detected across different map-making algorithms.

Therefore, it is possible to state that, within the MFs sensitivity in P^2 , no deviation from primordial Gaussianity and statistical isotropy has been detected in the Planck CMB polarisation maps within the adopted confidence mask.

7 CONCLUSIONS

MFs have been widely applied to the analysis of CMB data (Schmalzing & Górski 1998; Planck Collaboration 2020d), but their application to polarisation has been limited so far. In this work, we introduce a generalised framework to compute the MFs on maps of the modulus

Table 1. Deviation of MFs computed on Planck SMICA and SEVEM CMB polarisation maps with respect to the ones of respective end-to-end simulations, in terms of normalised χ^2 , probability to exceed, and σ .

		χ^2	$P_{\text{exc}} (\%)$	σ
V_0	SMICA	1.012	44.7	0.04
	SEVEM	0.993	47.0	-0.07
V_1	SMICA	1.010	47.7	0.02
	SEVEM	1.144	17.0	0.85
V_2	SMICA	0.812	86.7	-1.10
	SEVEM	1.084	30.7	0.42

of the polarisation ($P^2 = Q^2 + U^2$). MFs are able to provide information complementary to that obtained from angular power spectra and, in particular, it is sensitive to deviations from the hypothesis of a Gaussian isotropic field.

Our main contributions are the following:

- We introduce a general formalism to predict the value of MFs for P^2 in the case of a Gaussian and isotropic field, justifying how the effects of the spin are negligible in the cosmological case.
- We implement and release Pynkowski, a public Python package to compute MFs on Healpix maps of any scalar field, such as CMB T and P^2 .
- We find that theoretical predictions are compatible with the computations on Gaussian isotropic P^2 CMB maps generated with the Planck best-fit angular power spectra.
- We apply the formalism to Planck polarisation modulus maps (SMICA and SEVEM); we find compatibility (with less than 1.1σ deviation in all cases) between their MFs and the ones computed on realistic end-to-end simulations which take into account the anisotropic noise residuals due to the scanning strategy of the satellite. We can conclude that we do not observe any hint for primordial non-Gaussianity or deviation from statistical isotropy in Planck CMB polarisation maps.

In the coming years, we expect new high-quality CMB polarisation observations from on-going or planned missions such as SPT (Sayre et al. 2020), LSPE (Addamo et al. 2021), Simons Observatory (Ade et al. 2019), CMB-S4 (Abazajian et al. 2022) and LiteBIRD (Hazumi et al. 2019). MFs can play a key role in the study of primordial statistical anisotropies or non-Gaussianities of these polarisation maps. Furthermore, MFs might be especially relevant in light of the large-scale intrinsic anisotropies that are being detected in multiple observables.

The introduced formalism may also be useful to study other complex spin maps, such as the ones associated to gravitational lensing. Typically studied lensing maps are convergence maps (κ), which are found to be highly non-Gaussian, as they are produced by the distribution of matter in the Universe. The formalism introduced in this work can be even used to analyse gravitational shear maps (σ), which could yield additional information.

Finally, MFs can be employed to study Galactic and extragalactic foregrounds, as they strongly deviate from a Gaussian distribution and are (in the Galactic case) highly anisotropic. MFs can complement other higher-order statistics that are already used to analyse foregrounds, such as peak statistics (Carrón Duque et al. 2019) or neural networks (Farsian et al. 2020). As an example of this synergy, in Krachmalnicoff & Puglisi (2021) they train a neural network to generate a high-resolution dust foreground map with a given shape of their MFs, as dust emission is highly non-Gaussian (Jung et al. 2018; Ben-David et al. 2015).

The Pynkowski Python package we have developed to study MFs is fully documented and can be found in <https://github.com/javiccarron/pynkowski>, along with examples of its use.

ACKNOWLEDGEMENTS

MM and NV acknowledge support by ASI/COSMOS grant n. 2016-24-H.0 and ASI/LiteBIRD grant n. 2020-9-HH.0. Part of this work was also supported by the InDark INFN project. DM acknowledges support from the MIUR Excellence Project awarded to the Department of Mathematics, Università di Roma Tor Vergata, CUP E83C18000100006.

REFERENCES

- Abazajian K., et al., 2022, [p. arXiv:2203.08024](https://arxiv.org/abs/2203.08024)
- Addamo G., et al., 2021, *J. Cosmology Astropart. Phys.*, 2021, 008
- Ade P., et al., 2019, *J. Cosmology Astropart. Phys.*, 2019, 056
- Adler R. J., Taylor J. E., 2007, *Random fields and geometry*. Vol. 80, Springer
- Aiola S., et al., 2020, *J. Cosmology Astropart. Phys.*, 2020, 047
- Andrews A., Jasche J., Lavaux G., Schmidt F., 2022, [p. arXiv:2203.08838](https://arxiv.org/abs/2203.08838)
- Barrow J. D., Hervik S., 2006, *Phys. Rev. D*, 73, 023007
- Bartolo N., Komatsu E., Matarrese S., Riotto A., 2004, *Phys. Rep.*, 402, 103
- Ben-David A., von Hausegger S., Jackson A. D., 2015, *J. Cosmology Astropart. Phys.*, 2015, 019
- Carrón Duque J., Buzzelli A., Fantaye Y., Marinucci D., Schwartzman A., Vittorio N., 2019, *Astronomy and Computing*, 28, 100310
- Chen X., 2010, *Advances in Astronomy*, 2010, 638979
- Chen Z., Yu Y., Liu X., Fan Z., 2020, *ApJ*, 897, 14
- Coles P., Barrow J. D., 1987, *Monthly Notices of the Royal Astronomical Society*, 228, 407
- Delabrouille J., Cardoso J. F., Patanchon G., 2003, *MNRAS*, 346, 1089
- Desjacques V., Seljak U., 2010, *Classical and Quantum Gravity*, 27, 124011
- Fantaye Y., Marinucci D., Hansen F., Maino D., 2015, *Physical Review D*, 91, 063501
- Farsian F., Krachmalnicoff N., Baccigalupi C., 2020, *Journal of Cosmology and Astroparticle Physics*, 2020, 017
- Gott III J. R., Park C., Juszkievicz R., Bies W. E., Bennett D. P., Bouchet F. R., Stebbins A., 1990, *The Astrophysical Journal*, 352, 1
- Grewal N., Zuntz J., Tröster T., Amon A., 2022, *The Open Journal of Astrophysics*, 5, 13
- Górski K. M., Hivon E., Banday A. J., Wandelt B. D., Hansen F. K., Reinecke M., Bartelmann M., 2005, *The Astrophysical Journal*, 622, 759
- Hartlap J., Simon P., Schneider P., 2007, *A&A*, 464, 399
- Hazumi M., et al., 2019, *Journal of Low Temperature Physics*, 194, 443
- Jung G., Racine B., van Tent B., 2018, *J. Cosmology Astropart. Phys.*, 2018, 047
- Kamionkowski M., Kosowsky A., Stebbins A., 1997, *Physical Review Letters*, 78, 2058
- Kasak J., Creswell J., Naselsky P., Liu H., 2021, *Phys. Rev. D*, 104, 023502
- Krachmalnicoff N., Puglisi G., 2021, *The Astrophysical Journal*, 911, 42
- Lan X., Marinucci D., Xiao Y., 2018, *Stochastic Processes and their Applications*, 128, 1294
- Lerario A., Marinucci D., Rossi M., Steconci M., 2022, [doi:10.48550/arXiv.2207.08413](https://arxiv.org/abs/10.48550/arXiv.2207.08413)
- Martínez-González E., Diego J. M., Vielva P., Silk J., 2003, *MNRAS*, 345, 1101
- Matsumura T., et al., 2014, *Journal of Low Temperature Physics*, 176, 733
- Naselsky P. D., Novikov D. I., 1998, *The Astrophysical Journal*, 507, 31
- Newman E. T., Penrose R., 1966, *Journal of Mathematical Physics*, 7, 863
- Peña G. A., Candlish G. N., 2022, *MNRAS*, 511, 2259
- Pitrou C., Pereira T. S., Uzan J.-P., 2008, *J. Cosmology Astropart. Phys.*, 2008, 004
- Planck Collaboration 2011, *A&A*, 536, A1
- Planck Collaboration 2020a, *A&A*, 641, A4

Planck Collaboration 2020b, *A&A*, **641**, A5
 Planck Collaboration 2020c, *A&A*, **641**, A6
 Planck Collaboration 2020d, *A&A*, **641**, A7
 Sayre J. T., et al., 2020, *Phys. Rev. D*, **101**, 122003
 Schmalzing J., Górski K. M., 1998, *Monthly Notices of the Royal Astronomical Society*, **297**, 355
 Tomita H., 1986, *Progress of Theoretical Physics*, **76**, 952
 Zaldarriaga M., Seljak U., 1997, *Phys. Rev. D*, **55**, 1830
 Zürcher D., Fluri J., Sgier R., Kacprzak T., Refregier A., 2021, *Journal of Cosmology and Astroparticle Physics*, **2021**, 028
 do Carmo M. P., 1976, *Differential geometry of curves and surfaces*. Prentice Hall

APPENDIX A: ROBUSTNESS TO CMB MAP-MAKING ALGORITHM

In Section 6.2 we showed the results when MFs are computed on CMB Planck polarisation maps and realistic end-to-end simulations, both produced by the SMICA cleaning algorithm, assuming primordial Gaussianity and statistical isotropy, obtaining a complete compatibility between them.

We perform the same analysis with the SEVEM reconstructed maps in order to verify that the results are robust to the specific method used to extract the CMB signal.

In Figure A1 we show the comparison between MFs of the Planck polarisation modulus map and the ones of realistic simulations obtained with the SEVEM pipeline. As with SMICA, we can observe full compatibility between them with deviations always within $\pm 2\sigma$ where σ represent the dispersion among the simulations. Therefore, we find no indication of primordial non-Gaussianity or deviations from statistical isotropy of the observed CMB polarisation modulus.

APPENDIX B: NOISE ANISOTROPY

Planck CMB polarisation maps are known to be affected by noise residuals which are significantly anisotropic due to the mission scanning strategy (Planck Collaboration 2011), as it can be seen in Figure 2. Some portions of the sky are better observed; this reduces the noise and, consequently, the variance of the map in these regions. This pattern is still present in the residuals of the SMICA and SEVEM CMB maps. As a consequence of this anisotropic observation of the CMB, MFs are expected to deviate significantly from the isotropic Gaussian prediction.

Since we are mainly interested in primordial CMB effects, we compare the MFs of Planck maps with the ones of simulations which include realistic noise residuals (see Section 6.2). However, it is also possible to study the effect of this anisotropic noise contamination by comparing the MFs of SMICA and SEVEM realistic simulations with the theoretical expected values under the Gaussianity and isotropy hypotheses computed considering the average value of μ among all simulations and using equation (3).

We follow an analogous procedure to the one in Section 6.2. The deviations of theoretical expectations with respect to MFs computed on SMICA end-to-end simulations are reported in Figure A2, while the results in terms of normalised χ^2 , probability to exceed, and σ are shown in Table B1 for both SMICA and SEVEM cases. The deviations are strongly significant at a level of $20 - 45\sigma$, detectable in all MFs and both component separation algorithms. It is remarkable that this strong deviation can be exactly reproduced by the realistic noise simulations (compare to Table 1, where noise+CMB simulations are perfectly compatible with observations). This result highlights the

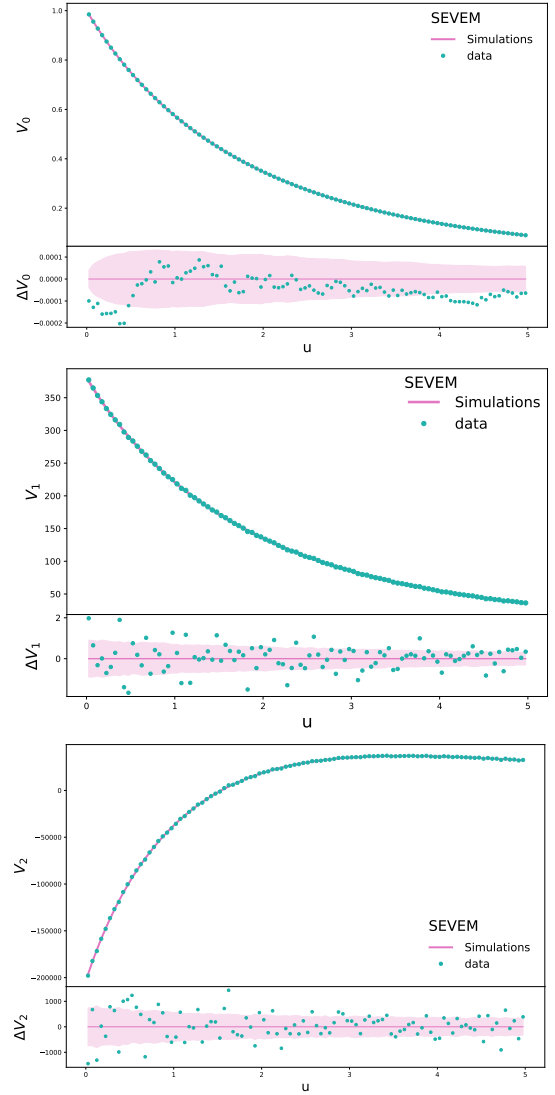


Figure A1. Minkowski Functionals of the Planck SEVEM released $P^2 = Q^2 + U^2$ maps (blue dots) and realistic end-to-end simulations (pink solid lines). First, second, and third MFs are shown (top to bottom), with the values and the residual with respect to the mean of simulations. The shaded pink region, representing the $\pm 1\sigma$ region obtained in simulations, is included in all plots.

Table B1. Deviation of realistic simulations from statistical isotropy hypothesis due to noise residuals, in terms of normalised χ^2 , probability to exceed, and σ .

		χ^2	$p_{\text{exc}} (\%)$	σ
V_0	SMICA	8.13	$3 \cdot 10^{-114}$	43.2
	SEVEM	9.03	$1 \cdot 10^{-131}$	45.0
V_1	SMICA	4.68	$6 \cdot 10^{-51}$	21.4
	SEVEM	6.20	$6 \cdot 10^{-78}$	29.1
V_2	SMICA	4.25	$1 \cdot 10^{-43}$	19.3
	SEVEM	4.85	$7 \cdot 10^{-54}$	22.2

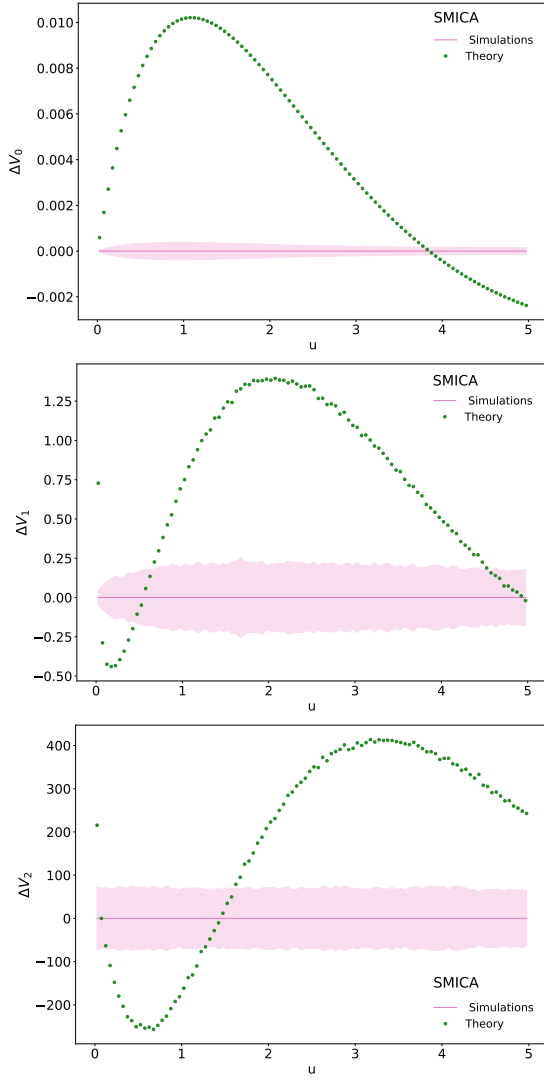


Figure A2. Deviations of theoretical Minkowski Functionals (green dots) in the Gaussianity and statistical isotropy hypotheses with respect to the ones computed on $P^2 = Q^2 + U^2$ of Planck SMICA realistic end-to-end simulations (pink). First, second, and third MFs are shown (top to bottom). The shaded pink region, representing the $\pm 1\sigma$ region obtained in simulations, is included in all plots.

potential of the application of MFs to future data, which will not be dominated by anisotropic noise as strongly as Planck maps. It also underlines the importance of calibration to realistic simulations, especially in polarisation data. Any possible future claim of detection of primordial non-Gaussianity or deviations from statistical isotropy of polarised CMB signal will have to be calibrated not only to realistic noise, but also to possible realistic residuals of galactic and extragalactic foregrounds.